On the Detection of Externally Forced Decadal Modulations of the Sahel Rainfall over the Whole Twentieth Century in the CMIP6 Ensemble

CASSIEN D. NDIAYE,[a,b] ELSA MOHINO,[c] JULIETTE MIGNOT,[b] AND SAIDOU M. SALL[a]

[a] LPAO-SF/Cheikh Anta Diop University, Dakar, Senegal
[b] LOCEAN/IPSL/Sorbonne University, Paris, France
[c] Departamento de Física de la Tierra y Astrofisica, Universidad Complutense de Madrid, Madrid, Spain

(Manuscript received 24 August 2021, in final form 20 June 2022)

ABSTRACT: The Sahel semiarid region was marked during the twentieth century by significant modulations of its rainfall regime at the decadal time scale. Part of these modulations have been associated with the internal variability of the climate system, linked to changes in oceanic sea surface temperature. More recently, several studies have highlighted the influence of external forcings during the dry period in the 1980s and the recovery around the 2000s. In this work we evaluate the internally and externally driven decadal modulations of Sahel rainfall during the entire twentieth century using a set of 12 models from phase 6 of the Coupled Model Intercomparison Project (CMIP6). We begin by proposing a physically based definition of Sahel rainfall that takes into account the southward bias in the location of the Sahelian ITCZ simulated by all the models. Our results show that the amplitude of the decadal variability, which is underestimated by most models, is mainly produced by the internally driven component. Conversely, the external forcing tends to enhance the synchrony of the simulated and observed decadal modulations in most models, providing statistically significant correlations of the historical ensemble mean with observations in 1/3 of the models, namely IPSL-CM6A-LR, INM-CM5-0, MRI-ESM2-0, and GISS-E2-1-G. Further analysis of the detection and attribution runs of the IPSL-CM6A-LR shows that anthropogenic aerosol dominate the decadal modulations of Sahel rainfall simulated by this model, suggesting that at least a part of the impact is ocean-mediated and operated through shifts in the ITCZ and the Saharan heat low.

KEYWORDS: Monsoons; Anthropogenic effects/forcing; Coupled models; Internal variability; Decadal variability; Tropical variability

1. Introduction

Monsoons are a very specific feature of tropical climate characterized by a strong seasonality of rainfall linked to changes in atmospheric circulation. They are energetically direct circulation systems closely coupled to the Hadley circulation in which moisture plays an important role (Kang et al. 2008; Schneider et al. 2014). Their seasonality is linked to changes in the interhemispheric energy balance that induce a meridional migration of the intertropical convergence zone (ITCZ) and associated rainfall over wide continental areas (Biasutti et al. 2018).

The West African monsoon (WAM) system reaches its maximum northward location during boreal summer, reaching the Sahel, a semiarid region limited to the north by the Sahara Desert and to the south by savannah. The Sahel rainfall regime is tightly linked to the West African monsoon, with a rainy season that typically lasts from July to September (JAS) (Thorncroft et al. 2011). The region's economy is based on rain-fed agriculture and grazing. Thus, a small shift in the position of ITCZ precipitation can cause dramatic variations in local precipitation (Kang 2020) and affect the economies locally. Moreover, the Sahel experienced a very wet period from the 1950s to 1960s followed by a long dry period in the 1970s and 1980s with important socioeconomic consequences (Kandji et al. 2006).

Numerous studies have been carried out to understand the low-frequency modulations of Sahel rainfall during the twentieth century (Biasutti and Giannini 2006; Hirasawa et al. 2020, 2022; Martin et al. 2014; Mohino et al. 2011; Villamayor et al. 2018; Hirasawa et al. 2020; Hirasawa et al. 2022; Zhang et al. 2022). In some of them, past modulations of Sahel rainfall at decadal time scales have been associated with changes of sea surface temperature (SST), in particular via those related to the Atlantic multidecadal variability (AMV) in the North Atlantic (e.g., Martin et al. 2014; Mohino et al. 2011; Rodríguez-Fonseca et al. 2011). The AMV has long been viewed as an internal mode of variability of the climate system (Zhang et al. 2019). Control simulations performed with state-of-the-art climate models can indeed simulate large decadal modulations of the North Atlantic SST and associated changes in Sahel rainfall (Zhang et al. 2019). Yet recent studies have highlighted the importance of external forcing for the generation of the AMV (Bellomo et al. 2018; Booth et al. 2012; Mann et al. 2021) and possibly thereby for the modulation of the WAM (e.g., Hirasawa et al. 2020, 2022; Zhang et al. 2022).

Low-frequency modulations of Sahel rainfall and in particular the rainfall decline during the second half of the twentieth century have been attributed in some studies to the greenhouse gas (GHG)-forced ocean warming (Biasutti and Giannini 2006). GHGs warm the global ocean resulting in a reinforcement of the evaporation in the tropics, which reduces tropical circulation in general and, in particular, the monsoonal flow (Gaetani et al. 2017). In addition, they can also induce a slowdown of the ocean meridional overturning

Corresponding author: Cassien D. Ndiaye, cassiendiabendiaye@gmail.com, cassien-diabe.ndiaye@locean.ipsl.fr

DOI: 10.1175/JCLI-D-21-0585.1

circulation (MOC), reducing thus heat transport in the North Atlantic, and forcing a tropical north–south temperature gradient (Biasutti and Giannini 2006). This yields an inhibition of the ITCZ northward migration. Yet, GHGs have also been shown to potentially influence WAM through direct radiative forcing, without the effect of SSTs. The partial recovery of Sahel rainfall around the 2000s is in particular also attributed to GHGs but via the direct response of the atmosphere (Dong and Sutton 2015). In this case, the leading mechanism is that the warming of the African continent induces a strengthening of the land–ocean thermal gradient, favoring moisture supply toward the continent and thus increased deep convection in the monsoon region (Dong and Sutton 2015; Gaetani et al. 2017; Haarsma et al. 2005).

On the other hand, although they suggest that in the future increased greenhouse gases could become a dominant driver of Sahel changes, Herman et al. (2020) argue that the effect of GHGs was not strong enough to explain the recovery of Sahel rainfall at the end of the twentieth century. Anthropogenic aerosols are another candidate to explain the recent Sahel rainfall decadal modulations (Booth et al. 2012; Giannini and Kaplan 2019; Herman et al. 2020; Hirasawa et al. 2020; Hirasawa et al. 2022; Zhang et al. 2022). As for GHGs, anthropogenic aerosols can act either directly or indirectly (via the SST) on the WAM. For example, the drought of the 1970s has been associated with the cooling of the North Atlantic due to anthropogenic aerosols (Booth et al. 2012), thus limiting the northward migration of ITCZ. The recent recovery in rainfall has also been attributed to the ocean-mediated effect of anthropogenic aerosols (Hirasawa et al. 2020). On the other hand, the so-called direct response to aerosol forcing (Dong and Sutton 2015) could influence precipitation in the Sahel without changing the sea surface temperature as they interact with shortwave (SW) and longwave (LW) radiation and modify the radiative and physical properties of clouds. Hirasawa et al. (2020) suggest that the dry period of the 1970s is due to a direct response of the atmosphere to anthropogenic aerosols (i.e., not ocean-mediated). Similarly, Dong and Sutton (2015) suggest the direct response to aerosols is one of the main factors explaining the recent rainfall recovery. So far, the attribution of rainfall modulations in the Sahel to external forcing is thus still under debate by the scientific community. The exact time scale on which these forcings may have an impact, from decadal to centennial, is also not clear.

The main objective of this study is to assess and quantify the effect of external forcings on decadal rainfall modulations in the Sahel region over the whole twentieth century. Using the amplitude of the variability and correlations computed over the whole twentieth century, we aim to assess whether external forcings have been strong enough to have had a significant impact on these decadal modulations over this full time period. Our approach is based on the analysis of the CMIP6 climate models. First (section 3), a general assessment of the effect of internal variability and of external forcings on decadal modulations of the Sahel rainfall throughout the whole twentieth century is provided across CMIP6 models that have at least 10 members of historical simulations. A more specific analysis of the role of the individual forcings is then proposed in the model IPSL-CM6A-LR (section 4). Information on data and method are given in section 2 and conclusions appear in section 5.

2. Dataset and methods

a. CMIP6 models

To assess the forced response of Sahel rainfall, three different types of simulations carried out in the framework of CMIP6 (Eyring et al. 2016) are used, namely piControl, historical, and DAMIP simulations.

The preindustrial simulations (piControl) are based on fully coupled models forced with non-evolving preindustrial conditions. These conditions are designed to be representative of the climate state before the beginning of the large-scale industrial period, and correspond to the reference year 1850. The recommended minimum duration for this experiment is 500 years (Pascoe et al. 2019). Our analysis is based on the longest possible piControl experiment for each model configuration (see Table 1). For each model, this simulation allows to characterize and to quantify internal decadal modulations, those not due to external forcing (which is held constant throughout the simulation) but only due to interactions among the climate system components.

Ensembles of historical experiments spanning from 1850 to 2014 are also used. For each model, individual historical members are forced by the observed changes in anthropogenic (aerosols, greenhouse gases, stratospheric ozone, and land use changes) and natural (solar and volcanic) external forcings (Gillett et al. 2016). To account for internal variability in the evolution of the climate over this period, several realizations of such experiments are performed for each model. These realizations differ by slight modifications of their initial conditions. Typically each member is started from a different date of the corresponding piControl experiment. Thus, each member has a unique trajectory that is influenced by both the external forcing and internal climate variability (e.g., Bonnet et al. 2021). For each model, the ensemble average of these experiments, called HistEns in the following, gives an estimation of the forced response of the climate system; the more members averaged, the more accurate this estimation (e.g., Kay et al. 2015). These ensembles, also called single-model initial-condition large ensembles (SMILEs), are increasingly used in several studies (e.g., Kay et al. 2015; Maher et al. 2021). In our study, in order to have a sufficient number of models and thus a multimodel view of the forced decadal modulations of Sahel rainfall as represented by the CMIP6 ensemble, we arbitrarily decide to use models that performed at least 10 historical simulations (more details in Table 1).

Finally, we also analyze four components of the Detection-Attribution Model Intercomparison Project (DAMIP simulations). These experiments are based on the setup of the historical simulations but constrained with forcing of only one origin: natural (Nat), greenhouse gases (GHG), anthropogenic aerosols (AA), and stratospheric ozone (Ozone), respectively

TABLE 1. Information on the CMIP6 models used in this study.

No.	Model name	Atmospheric resolution (lon × lat)	No. of members of historical simulations	No. of members of DAMIP simulations	Years of piControl simulations	Variant label of the experiments	References
1	ACCESS-ESM1-5	1.875° × 1.25°	40	3 (for GHG, AA, Nat, no Ozone)	1000	r[1–40]i1p1f1	Ziehn et al. (2020)
2	CanESM5	2.8° × 2.8°	25	25 (GHG), 15 (AA), 25 (Nat), 10 (Ozone)	1000	r[1–25]i1p1f1	Swart et al. (2019)
3	CESM2	1.25° × 0.9°	11	3 (GHG), 2 (AA), 3 (Nat), no Ozone	1200	r[1–11]i1p1f1	Danabasoglu et al. (2020)
4	CNRM-CM6-1	1.4° × 1.4°	29	10 (GHG, AA, Nat)	500	r[1–29]i1p1f2	Voldoire et al. (2019)
5	EC-Earth3	0.7° × 0.7°	17	—	501	r[1–17]i1p1f1	Döscher et al. (2022)
6	GISS-E2-1-G	2.5° × 2°	11	5 (GHG, AA, Nat, no Ozone)	851	r[1–11]i1p1f2	Miller et al. (2021)
7	INM-CM5-0	2° × 1.5°	10	—	1201	r[1–10]i1p1f1	Volodin et al. (2018)
8	IPSL-CM6A-LR	2.5° × 1.27°	32	10 (GHG, AA, Nat, Ozone)	1200	r[1–32]i1p1f1	Boucher et al. (2020)
9	MIROC6	1.4° × 1.4°	50	3 (GHG), 10 (AA), 50 (Nat), 3 (Ozone)	800	r[1–50]i1p1f1	Tatebe et al. (2019)
10	MPI-ESM-1-2-LR	1.875° × 1.875°	10	—	1000	r[1–10]i1p1f1	Mauritsen et al. (2019)
11	MRI-ESM2-0	1.125° × 1.125°	10	5 (GHG, AA, Nat), 3 (Ozone)	701	r[1–10]i1p1f1	Yukimoto et al. (2019)
12	NorCPM1	2° × 2°	30	—	500	r[1–30]i1p1f1	Bethke et al. (2021)

[more details in Gillett et al. (2016)]. The CMIP6 protocol spans the time range 1850–2014. Each experiment is performed several times, as for the historical ensemble. Note that the DAMIP experiments only forced by land use do not exist (Gillett et al. 2016). Experiments proposed in the Land Use Model Intercomparison Project (LUMIP; Lawrence et al. 2016) are not directly comparable. The effect of this forcing will thus not be addressed specifically here. As shown in Table 1, relatively fewer members are usually run for each model in DAMIP configurations. It is thus generally difficult to attribute robustly the detected forced modulations.

b. *Observations*

In this study, three observational datasets from different sources are analyzed to evaluate the model's capacity to reproduce the observed climate modulations. First, the monthly land surface precipitation datasets with a spatial resolution of 0.5° from the Climate Research Unit, version 4.01 (CRU TS 4.01; Harris et al. 2020) for the period 1901–2016 and GPCC, version V2018.05 (GPCC V2018.05; Meyer-Christoffer et al. 2018) covering the period 1891–2016 are used. These datasets differ by the weather stations used and the methodology applied to derive the gridded products. In particular, GPCC uses more weather stations while the approach of CRU gives greater temporal fidelity (Undorf et al. 2018). We also use SST from the Hadley Centre Sea Ice and Sea Surface Temperature reanalysis dataset (HadISST1; Rayner et al. 2003) covering the period from 1870 to 2015 with a spatial resolution of 0.5°.

c. *Methods*

The temporal coverage of the observational data and the model simulations differ, but all data cover the period 1901–2014 on which our analysis is based.

To extract the decadal-scale modulations, we apply successively a high-pass and a low-pass filtering to both observed and simulated time series. The high-pass filtering aims at removing possible centennial variability that has been detected in several recent climate simulations (e.g., Jiang et al. 2021; Voldoire et al. 2019). It consists of the removal of the linear trend calculated from a least-squares fit to a first-order polynomial of the corresponding 114-yr-long time series. A low-pass Butterworth filter of order 10 with a 10-yr cutoff is then applied. The signals obtained this way are called "decadal modulations" in the rest of this study.

Our analysis of the effect of internal variability and external forcing on the decadal modulations of the Sahel rainfall is twofold. On the one hand, it evaluates the amplitude of the signals by calculating the standard deviation of the time series. On the other hand, it considers the synchrony of the simulated time series with observations using anomaly correlation coefficients (ACC). Unless stated otherwise, statistical significance of ACC is assessed using nonparametric approaches. Indeed, the number of degrees of freedom is probably limited in our 114-yr-long low-pass filtered time series and difficult to estimate. More details are given in the corresponding results sections.

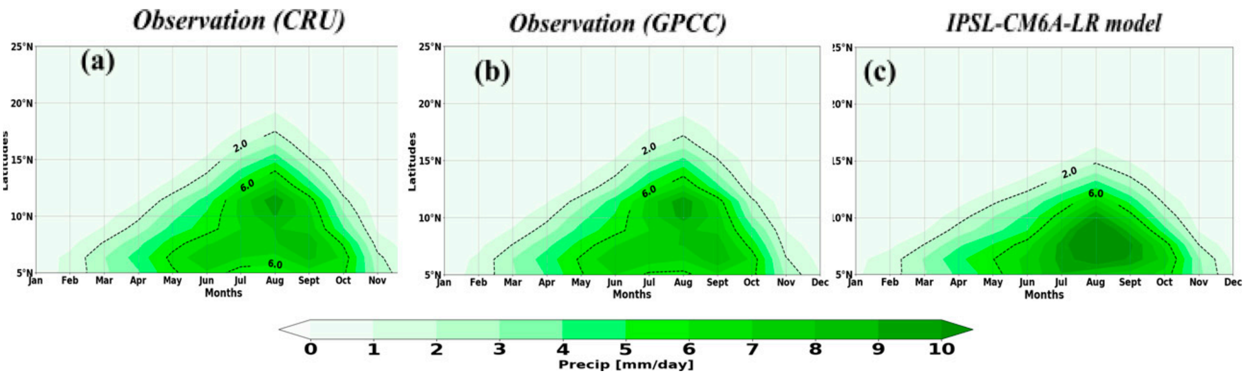

FIG. 1. Observed and simulated precipitation over North Africa (mm day^{-1}) averaged over the period 1901–2014. Rainfall annual cycle (color and contour) averaged over the longitude range 20°W–20°E from the (a) Climatic Research Unit (CRU) and (b) Global Precipitation Climatology Center (GPCC) observational datasets and (c) a historical simulation of the IPSL-CM6A-LR model.

3. Contribution of the internal variability and external forcings on decadal modulations of the Sahel rainfall in the CMIP6 ensemble

a. An adaptable definition of the Sahel region

The rainfall annual cycle observed over West Africa is presented in Figs. 1a and 1b by zonally averaging the rainfall over the longitudinal domain 20°W–20°E. Note that in all these analyses, rainfall is only considered over land grid points. The West African monsoon reaches its northernmost position (around 15°N) in August: the Sahelian phase of the monsoon (Thorncroft et al. 2011). This phase is intense during the months of July, August, and September (JAS) corresponding to the period when the Sahel receives the majority of its annual rainfall, here defined as the monsoon season. Compared to observations, CMIP6 simulations from 12 models simulate reasonably well the observed annual cycle, although the maximum rainfall in August is most often abnormally shifted southward (not shown). As an example, Fig. 1c shows that in the IPSL-CM6A-LR model it reaches only around 7°N. The mean Sahel rainfall over the summer period (JAS) also highlights this bias in all models (Fig. 2). This feature is consistent with previous findings for models participating in CMIP5 (Monerie et al. 2020b) and the more recent CMIP6 intercomparison exercises (Klutse et al. 2021).

Given the zonal orientation of summer rainfall, the longitudinal limits of the Sahel region may vary depending on the studies (Biasutti 2019; Dong and Sutton 2015; Gaetani et al. 2017). In this work, they are taken as 20°W–20°E. The meridional limits of the Sahel region are generally fixed to 10°–20°N. In Fig. 2 the latitudinal extension of the Sahel region is analyzed more carefully in order to account for the southern shift of the rainfall pattern in the CMIP6 models. In the observation datasets, the northern limit of the so-called Sahel region (20°N) corresponds to the latitude where no more rain occurs

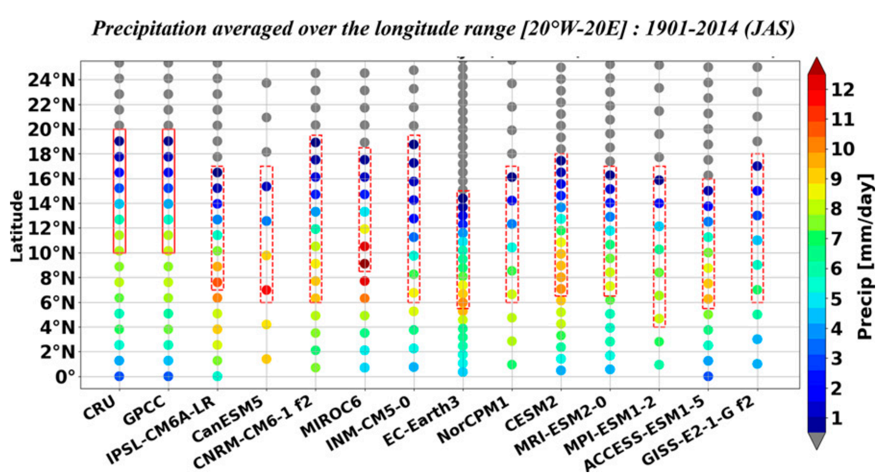

FIG. 2. Observed and simulated precipitation (mm day^{-1}) over 1901–2014 of the summer season (JAS). Precipitation averaged over the longitude range 20°W–20°E as a function of latitude from the CRU and the GPCC observational datasets as well as from the first member of the historical ensemble of each selected model. Full and dashed boxes represent the meridional limit of the Sahel region for observation and models, respectively, following a physical definition (see the text for details).

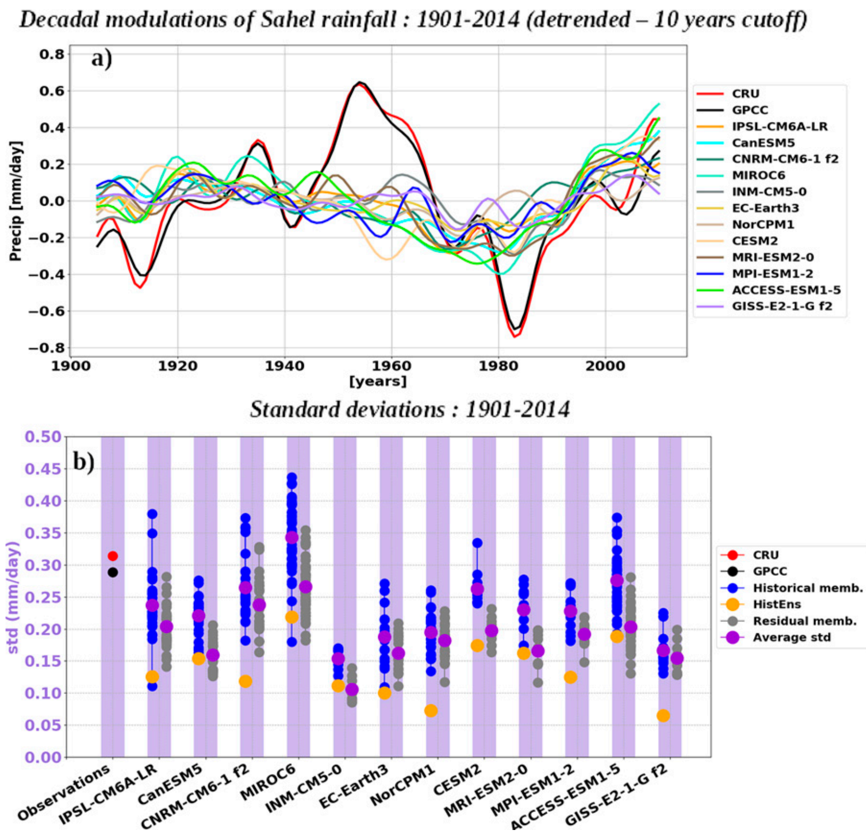

FIG. 3. Observed and simulated decadal variability of Sahel rainfall (JAS) for the period 1901–2014. (a) Time series of anomalous Sahel rainfall (mm day^{-1}) computed with respect to the entire 1901–2014 study period. Red and black indicates the CRU and GPCC observed datasets respectively; other colors represent HistEns of 12 CMIP6 models. (b) Standard deviations (std) from CRU (red dots) and GPCC (black dots) observations, from each historical member (blue) and residual members (gray) obtained by subtracting HistEns from each historical member for each CMIP6 model. Purple and orange dots represent the mean standard deviation of the members and the standard deviation of HistEns, respectively.

(<0.5 mm day^{-1}) over the monsoon season. The southern limit of the traditional definition of the Sahel rainfall corresponds to the maximum of summer rainfall (8.0 mm day^{-1} at 10°N). This corresponds to the solid red box in the first two columns of Fig. 2. In the other columns of Fig. 2, we apply these physically based meridional limits to the simulated zonally average rainfall for each model. Note that in order to mimic observations, for which only one realization is available, while internal variability weakly impacts the climatological mean computed over 30 years as in Fig. 2 (not shown), only the first member of the historical ensemble of each model is used in Fig. 2. Placing the southern limit for the Sahel region at the latitude where the maximum rainfall is simulated for each model and the northern limit at the latitude corresponding to the limit of the rainy zone as in the observations yields the latitudinal location of this region for each model shown in Fig. 2 (red box). The Sahel region so defined in each model is shifted southward as compared to the observations. This definition will be used in the remainder of this study. Note that although it is more physically based than the classical definitions, the observed maximum precipitation remains overestimated in almost all models, except in the NorCPM1, GISS-E2-1-G, and MPI-ESM1-2 models (Fig. 2).

b. *Analysis of decadal modulations of Sahel rainfall in CMIP6 models*

Observed and simulated low-frequency modulations of Sahel rainfall are analyzed in Fig. 3. Both observation datasets show multidecadal modulations during the twentieth century with negative anomalies at the beginning of the century, positive ones in the 1950s and 2000s, and negative ones again in the 1980s, in accordance with previous studies (Berntell et al. 2018; Lebel and Ali 2009; Nicholson 1983; Fig. 3a). The forced modulations of the Sahel rainfall as diagnosed from the ensemble mean of the historical sets of CMIP6 climate models also show signals at the decadal to multidecadal time scale. Models generally agree that the period around 1920–30 was anomalously wet, and the period 1970–80 relatively drier. The rainfall recovery toward the 2000s also tends to be relatively well reproduced by the forced response. The agreement among models and observations at the decadal time scale requires more quantitative metrics to be clearly assessed.

We analyze first the simulated and observed amplitude of variability by the standard deviation values in Fig. 3b. The standard deviation amounts to 0.31 mm day^{-1} for CRU and 0.29 mm day^{-1} for GPCC. Only the historical members of the models IPSL-CM6A-LR, CNRM-CM6-1, MIROC6, CESM2, and ACCESS-ESM1-2 show a range of standard deviations (blue dots in Fig. 3b) that include the observed values. The latter are, however, higher than the mean standard deviation of the different models used, except for the MIROC6 model, which amounts to 0.34 mm day^{-1}. It is also higher than the mean value of the standard deviations of all historical members of all models (average of all blue dots in Fig. 3b), which is 0.23 mm day^{-1}. This analysis shows that the amplitude of observed Sahel rainfall is underestimated by the majority of CMIP6 models used. This is a general feature of coupled models already highlighted in earlier exercises of intercomparison (e.g., Rodríguez-Fonseca et al. 2011; Joly et al. 2007; Kucharski et al. 2013; Biasutti 2013) and thus does not seem to have improved in CMIP6. This could be related to the accuracy with which feedback processes, like vegetation–atmosphere feedbacks, are parameterized (Giannini et al. 2003; Zeng et al. 1999) or to the coarse resolution that does not allow for explicit simulation of deep convection (Vellinga et al. 2016).

The amplitude simulated by the models results from the response of precipitation to both internal variability and external forcings. Each of these may be individually underestimating the observed amplitude. One can note that the estimated forced modulations of the CMIP6 models are much smaller than the observed variability (Fig. 3a). This is quantified in Fig. 3b: the standard deviations of the historical ensemble mean (HistEns) of the different models (orange dots in Fig. 3b) are systematically smaller than the observed standard deviation and the mean standard deviation of the individual historical members. In addition, the mean value of the standard deviations of the HistEns of all models, which is 0.13 mm day^{-1} (average of all orange dots in Fig. 3b), is also smaller than the observed standard deviation and the mean value of the standard deviations of all historical members of all models. This indicates that external forcing cannot generate the observed amplitude of variability. This would be consistent with a part of variability being produced internally by the climate system. To assess the role of the latter, we diagnose the residual internal variability in each individual simulation by subtracting the HistEns of the respective models. The standard deviation of residual variability is shown in Fig. 3b (gray dots). Compared to HistEns, it tends to be closer to that of historical members and observations. This is true for all models except INM-CM5-0 for which the standard deviation of the HistEns is above the average residual one. The mean value of the standard deviations of residual variability of all models, which is 0.18 mm day^{-1} (average of all gray dots in Fig. 3b), is close to that of all historical members of all models and observations. This analysis confirms the role of internal variability in setting the amplitude of the total variability. It follows that the fact that individual historical members tend to underestimate the observed amplitude might thus be due to an underestimated amplitude of the simulated internal variability, as suggested in the North Atlantic region by Kim et al. (2018) and Yan et al. (2019).

To quantify the synchrony of the simulated modulations of Sahel rainfall in the CMIP6 models, we compute the ACC of the rainfall time series over the full 1901–2014 period with observations. Since CRU and GPCC modulations are very similar, we focus here on the CRU dataset only. Correlation coefficients of the individual historical members shown in blue marker in Fig. 4a for each model may be positive or negative, except for those of the INM-CM5-0 and MRI-ESM2-0 models, which are all positive. The average correlation is, however, positive and strictly above zero for all the models, which suggests that for each of these models, historical members are on average relatively synchronized with the observations. To disentangle between the external and internal influences, we evaluate the correlations for the residual variability for each individual member. The range of correlations of the individual members is very wide, with both positive and negative values, which suggests that the internal variability could, by chance, be synchronized with observations. However, the average correlation of the residual members of various models is approximately zero, suggesting no systematic influence of the internal variability on the synchrony of the average modeled response with observed modulations. In all the models, the forced response as diagnosed from HistEns has a higher correlation than the average correlation of the individual historical or residual members. This further indicates that the effect of external forcing alone tends to systematically enhance the synchrony of the average response with the observed modulations. However, this does not mean that the average response is significantly correlated with the observations.

To gain confidence in the effect of external forcing in terms of synchrony the variability, the significance of the HistEns correlations is quantified by a statistical test based on the long piControl simulation. In practice, for each model, we extract portions of 114 years (length of the historical period) of the long piControl simulation starting from randomly chosen dates. The number of extracted portions corresponds to the size of the historical ensemble of each model (see Table 1). These portions are furthermore averaged and called piCtrlEns in the following. We have applied exactly the same statistical treatment to these piCtrlEns as for the HistEns (section 2). Since there is no physical reason why an ensemble average of piControl simulations would be synchronized with observations, the correlation of piCtrlEns and observations is considered as noise. In Fig. 4b we show for each model the probability density function (PDF) of the correlation of 5000 combinations of piCtrlEns with the CRU time series of Sahel rainfall (gray shading). We note that the PDFs could be subjected to sampling uncertainty, meaning that they can vary when the 5000 combinations are resampled, or if only the last 500 years of the piControl simulations are sampled. Yet further analysis showed that this effect is small and does not change the results shown below (not shown).

The significance of the correlation of HistEns with observations is evaluated against this PDF based on piCtrl segments for each model. Correlation of the forced ensemble is considered significant if it exceeds the 2.5% extreme maximum and

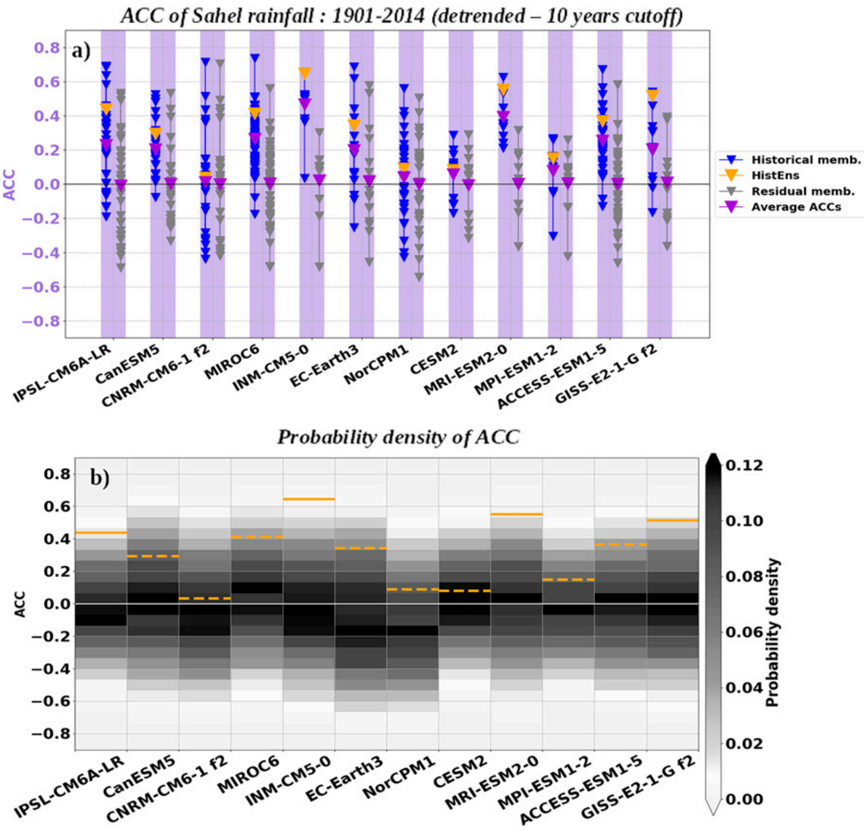

FIG. 4. ACC between observed and simulated decadal variability of Sahel rainfall (JAS) for the period 1901–2014. (a) ACC between observations from the CRU dataset and each historical member (blue marks), HistEns (orange marks), and residual members (gray marks) obtained by subtracting HistEns and each historical member for each CMIP6 model. Purple marks represent the mean ACC average for the different historical members. Purple and orange marks represent the mean ACC of the members (historical and piControl) and the ACC of HistEns from historical experiments of each model, respectively. (b) Probability density function of ACC between observations from the CRU dataset and 5000 combinations of piCtrlEns of each CMIP6 model. Full and dashed orange lines represent correlations between observations from CRU and HistEns from historical experiments of each model and significant correlations at the 95 % level, respectively. More information on the significance test used in the section 3b where this figure is described.

minimum values of the PDF constructed with the unforced ensemble. Using this approach, significant correlations are found for four (i.e., one-third) of the models: IPSL-CM6A-LR, INM-CM5-0, MRI-ESM2-0, and GISS-E2-1-G, with values of 0.44, 0.65, 0.55, and 0.51, respectively. The forced signal in CanESM5, CNRM-CM6-1, MIROC6, EC-Earth3, NorCPM1, CESM2, MPI-ESM1-2, and ACCESS-ESM1-5 is, on the other hand, insignificantly correlated with observations. The insignificant or significant synchrony of the forced decadal modulations of the Sahel rainfall with observations in these models may be due to an incorrect or insufficient response to the external forcings or the internal variability not sufficiently averaged out. For CNRM-CM6-1, NorCPM1, CESM2, and MPI-ESM1-2, the difference between the HistEns ACC scores and the average ones obtained from the historical members and the residual members is relatively weak (Fig. 4a). This suggests that the external forcing does not provide any synchrony with the observations for these models. External forcings on the other hand clearly improve the correlation of Sahel rainfall with observations in CanESM5, MIROC6, EC-Earth3, and ACCESS-ESM1-5 (Fig. 4a), although not sufficiently to make it significant. For IPSL-CM6A-LR, INM-CM5-0, MRI-ESM2-0, and GISS-E2-1-G, the significant correlation at 95% of the forced response suggests that it is very unlikely that the internal variability could be explaining the correlations of the ensemble average of these models with observations. One cannot rule out at this stage that the forced response is overestimated in these models, or that it might be due to an incorrect response, although we believe this last possibility is less probable.

Given that models tend to show reduced variance in the HistEns with respect to the average variance (Fig. 3b), one could wonder if the four models that show statistically significant ACC scores could be suffering from the signal-to-noise paradox (Scaife and Smith 2018): Many models are better capable of predicting observations than of predicting themselves, especially over the Atlantic region. We have tested if this is indeed the case by calculating the ratio of the predictable component (RPC) as defined in Eq. (1) of Weisheimer et al. (2019), that is, the ratio between the predictable component of the real world and the predictable component of a model. The predictable component of the real world is estimated by the square root of the observed variance explained by the HistEns (the correlation values in Fig. 4a, orange triangles). The estimation of the predictable component of each model is derived by the square root of the ratio of the model signal (square of orange circles in Fig. 3b) to the total variance of the simulations (for each model, addition of the square of the orange circle and the average of the squares of the purple circles of the residual column in Fig. 3b). The RPC is 1.34 for the GISS-ES-1-G model, which suggests it suffers to some degree from the paradox, as the significant correlation of this model is inconsistent with its small predictable signal. However, for the IPSL-CM6A-LR, INM-CM5-0, and MRI-ESM2-0 models, the RPC is between 0.79 and 0.89, suggesting that their correlation with observations is relatively consistent with the model's own behavior, with some degree of underestimation for the predictable signal in the observations or/and an overestimation of the model's own predictable signal.

To better understand the origin of the forced response in the four models for which the forced signal is significantly correlated with the observations, we turn our attention to the role played by the individual forcings. Unfortunately, at the time of writing, the INM-CM5-0 model has not run in DAMIP configuration, and MRI-ESM2-0 and GISS-E2-1-G only have five or fewer members for each forcing. This is presumably too little to draw robust conclusions. We thus finally propose a specific analysis based on the IPSL-CM6A-LR model alone, which proposes 10 members for each DAMIP configuration.

4. Attribution of forced decadal modulations of Sahel rainfall in the IPSL-CM6A-LR model

a. Influence of the individual forcings

The IPSL-CM6A-LR Earth system model is the global coupled ocean–atmosphere general circulation model developed by the Institut Pierre-Simon Laplace (IPSL) as part of CMIP6 (Boucher et al. 2020). It is an improved version of the IPSL-CM5B model used in CMIP5. The low spatial resolution (LR) version of the IPSL-CM6A model is used in this study and corresponds to the medium spatial resolution (MR) of IPSL-CM5A. The model is composed of version 6A-LR of the LMDZ atmospheric model (Hourdin et al. 2020), version 3.6 STABLE of the NEMO ocean model, and version 2.0 of the ORCHIDEE land surface model.

As previously shown (Fig. 4), the ensemble mean of summer Sahel rainfall computed from the 32 members of the historical experiment (called HistEns32 in the following), is significantly correlated with the observed Sahel rainfall modulations (0.47 with CRU and 0.43 with GPCC) for the entire twentieth century. The time series are reproduced for this model only in Fig. 5a for clarity. Spatially, the correlation with the Sahel rainfall index from CRU is high and positive over the western Sahel, particularly over Senegal (Fig. 5c). For the statistical test of the ACC pattern, the same approach as defined in the previous section is used but here the piCtrlEns PDF based on 32 members taken randomly through the long piCtrl simulation (called piCtrlEns32 in the following) is calculated at each grid point. These correlations are significant at the 95% level in the western Sahel and a part of the eastern Sahel. They are also relatively high in the far eastern Sahel (30°–35°E), outside of our region of interest. The mechanisms responsible for these latter correlations are left for separate studies. This analysis indicates that in this model, the influence of external forcing on the synchrony of the observed modulations of the Sahel rainfall is most prominent in the western part of the Sahel region.

To better analyze the effect of the individual external forcing on the observed decadal modulations of rainfall in the Sahel, we select the first 10 historical members, whose initial conditions correspond to the ones from which the 10 members of each of the DAMIP experiments of this model were started. The ensemble average calculated using these first 10 members will be referred to hereinafter as HistEns10. The decadal modulations in HistEns10 (blue in Fig. 5a) also show high positive correlations (between 0.60 and 0.80) with the CRU time series in the western Sahel and a part of the eastern Sahel (Fig. 5b). The HistEns10 Sahel time series is strongly correlated to observations with ACC values of 0.63 with CRU and of 0.61 with GPCC. Using the statistical test detailed in the previous section but with a piCtrlEns PDF based on 10 members randomly chosen, these correlations are statistically significant (not shown). To gain further confidence in these correlations and in particular in the representativity of the 10 first historical members within the initial ensemble of 32, we additionally computed HistEns10 PDFs by calculating the distribution of correlations between the CRU observed time series of Sahel rainfall and 5000 ten-member averages of randomly picked historical members from the 32 possibilities (Fig. 6, blue bars). This distribution is compared to a PDF similarly built but using the 32 portions of the piControl experiment that start from the 32 dates used as initial conditions in the various historical members (Fig. 6, gray bars). Both PDFs are statistically distinguishable at the 95% confidence level using the Kolmogorov–Smirnov test. This confirms that in this model external forcing significantly acts to shift the decadal modulations of the Sahel rainfall toward the observations, and that this effect can be seen even with ensembles of only 10 members. Internal variability strongly competes with this effect, as can be seen from the relatively wide spread of the HistEns10 PDF obtained with randomly selected ensembles of 10 forced members. One can nevertheless see that the width of the PDF is reduced in the forced ensemble, suggesting that the external forcing contributes to reduce the uncertainty of the decadal modulations of the Sahel rainfall. In addition, the median of the HistEns10 PDF is similar to the correlation of the HistEns32 (orange line). The HistEns10, derived

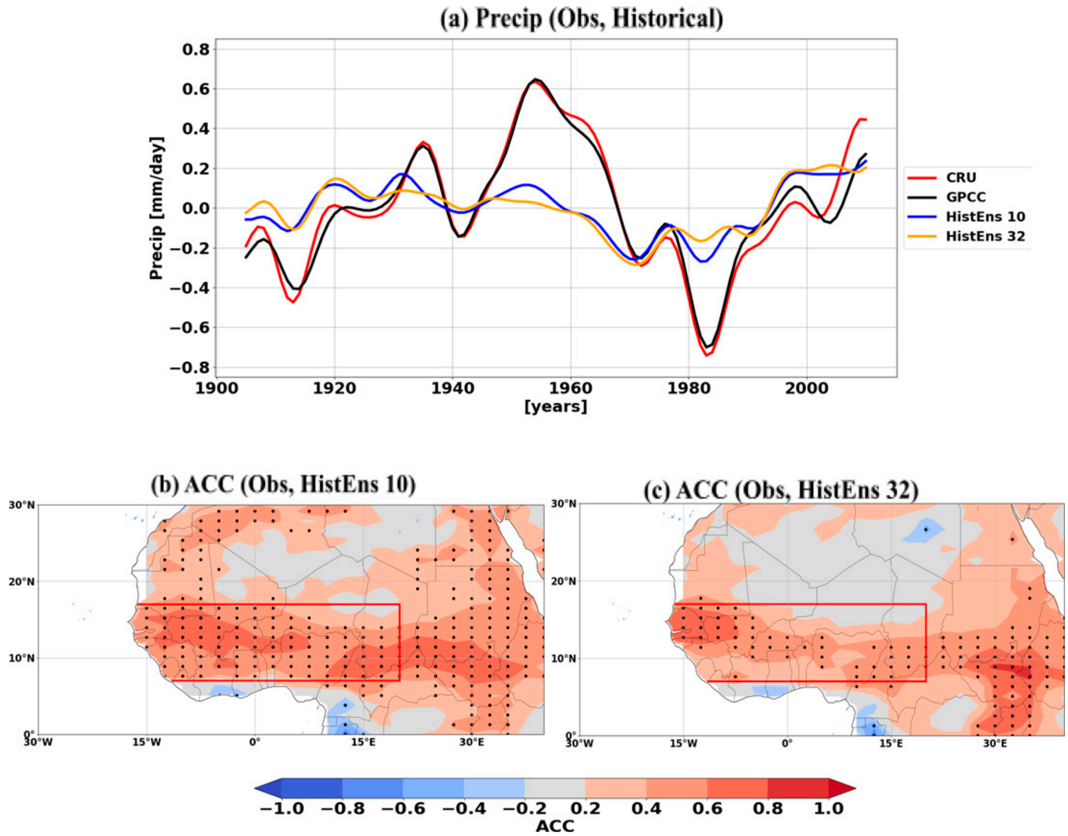

FIG. 5. Decadal variability of Sahel rainfall (JAS) for the period 1901–2014. (a) Time series of anomalous Sahel rainfall (mm day^{-1}) computed with respect to the 1901–2014 study period. Red and black indicate CRU and GPCC observed datasets respectively; blue and orange indicate the ensemble mean of 10 and of 32 members, respectively. The bottom panels represent the anomaly correlation coefficient (ACC) between the decadal residual of the observed (CRU) index and the decadal variability of the simulated summer precipitation at each grid point obtained in HistEns from (b) the 10 first members and (c) all 32 members of the historical experiment. The significant correlations at the 95 % level are marked by asterisks (*). More information on the significance test used in the sections where this figure is described.

from the 10 first historical members (blue line in Fig. 6), is relatively strongly correlated to observations as compared to the correlation inferred from HistEns32 and the HistEns10 PDF, but the analysis above gives confidence in the robustness of this correlation.

We thus now turn our attention to understanding the synchrony of the decadal modulations of the Sahel rainfall in the model. For this, we analyze the contribution of the different external forcings. Figure 7a shows a high and significant correlation between HistEns10 and the response to AA forcing only. AA forcing explains 60% of HisEns10 variance (ACC = 0.75). In addition, the standard deviation of Sahel precipitation due to AA forcing amounts to 90% of that of the HistEns average signal. Conversely, the Nat, Ozone, and GHG forcings yield modulations of the Sahel rainfall that are insignificantly correlated with the total forced response. The standard deviation of the Sahel precipitation in these ensembles of forced simulations is weaker than the total standard deviation of precipitation time series in the historical run (blue values in Fig. 7a). The grid point correlation confirms the strong effect of AA on the synchrony of the forced decadal signal in the model (Fig. 7c) as opposed to Nat, GHG, and Ozone (Figs. 7b,d,e). This result suggests that forced decadal modulations of Sahel rainfall during the twentieth century is primarily explained by AA forcing in this model. This result completes recent studies suggesting the role of AA on specific periods of the twentieth century (Herman et al. 2020; Hirasawa et al. 2020, 2022; Zhang et al. 2022). Here, it is shown that this role is significant when averaged over the whole century. To clarify mechanisms, the rest of this study focuses on the ocean-mediated influence.

b. *Influence of the SST decadal modulations*

As stated in the introduction, the effect of anthropogenic aerosols on Sahel rainfall could be the result of a direct radiative response and/or could be mediated through SST changes. To evaluate the potential role of the ocean-mediated mechanism on average over the whole twentieth century, we computed the correlation between the Sahel decadal rainfall index and the decadal modulations of the SST at each grid

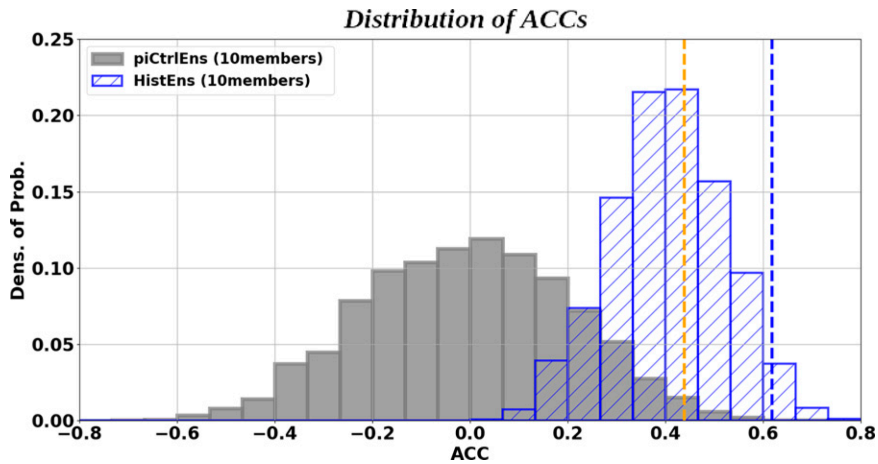

FIG. 6. PDF of ACC between observation from the CRU dataset and 5000 combinations of 10 members taken randomly among the 32 members of the historical experiment (blue) and among the 32 portions of 165 years starting from the same 32 dates of the piControl experiment (gray) used as initial conditions in the various historical members. Blue and orange vertical lines represent the correlations between the observation and HistEns from 10 first members and from all 32 members of the historical experiment, respectively.

point in observations and in the model (Fig. 8, top panels). Note that at each grid point, the same approach as defined in section 2c for extracting the decadal-scale modulation is also applied to the SST before the calculation of the correlation. The significance of the correlation is quantified here with a nonparametric random-phase test of Ebisuzaki (1997), as in Yan et al. (2019), which takes into account the autocorrelation of the time series. Significance is given with respect to a p value of 0.05. The pattern of correlation in observations (Fig. 8a) shows an interhemispheric structure of SST associated with enhanced precipitation, with positive correlations in the Northern Hemisphere and negative ones in the Southern Hemisphere. In the North Pacific and Atlantic in particular, including the Mediterranean Sea, the correlations are positive and statistically significant at the 95% confidence interval. Several studies have already shown an influence of SST anomalies on the low-frequency variability of precipitation in the Sahel (Rowell 2003; Mohino et al. 2011; Rodríguez-Fonseca et al. 2015). In the Southern Hemisphere, negative correlations are significant in some areas in the tropical and subtropical band, and in particular in the Indian Ocean. This pattern is consistent with Martin et al. (2014, their Fig. 2) and Lu (2009, their Fig. 9).

This observed SST–Sahel rainfall relation may be the result of both internal and forced compounds. In the model, we can explore the forced and internal mechanisms separately, as long as we suppose that they can be separated. We first focus on the internal relationship between SSTs and Sahel rainfall using the 1200-yr piControl simulation (Fig. 8b). The SST pattern associated with Sahel rainfall decadal modulations is quite similar to the one found in observations in the Northern Hemisphere yet with weaker correlation values (Fig. 8a). This is consistent with several studies that have shown a clear influence of AMV on the decadal modulations of the Sahel rainfall (e.g., Martin et al. 2014; Mohino et al. 2011; Rodríguez-Fonseca et al. 2011). This pattern indicates that the internal variability in the model is able to induce changes in Sahel rainfall via a teleconnection with North Atlantic SSTs comparable to observations. The pattern resembles the AMV pattern in the model (Boucher et al. 2020). Note that in the historical experiments of this same model, AMV computed in individual members is less correlated with the observed AMV than the ensemble mean HistEns (except for 3 members out of 32; not shown). Thus the synchrony of the simulated HistEns AMV with the observed one is largely due to external forcings (not shown). It is therefore unlikely that internal AMV in the model may induce the synchrony between the model's Sahel monsoon and the observations highlighted in Fig. 4.

The SST in the Mediterranean Sea also shows a significant correlation with the WAM decadal modulations both in the observations and in the piControl simulation. This could suggest a causal link as well (Park et al. 2016; Rodríguez-Fonseca et al. 2011; Rowell 2003). The PDO-like pattern in the Pacific in Fig. 8b could be due to an influence of the AMV on the Pacific decadal oscillation (PDO) in the model, as described in Boucher et al. (2020), or reflect an influence of the PDO on Sahel rainfall (Villamayor and Mohino 2015). We also note that in the control simulation, correlations in the Southern Hemisphere are statistically significant only in some limited areas and in particular not in the Indian Ocean, as opposed to what is detected in the observations (Fig. 8a).

In terms of mechanisms, the Atlantic SST pattern induces a northward shift of the ITCZ over the Atlantic basin and adjacent continental areas (not shown), in agreement with previous works (Folland et al. 1986; Martin et al. 2014; Zhang et al. 2019). Over the land, it is also expected to modulate the summer Saharan

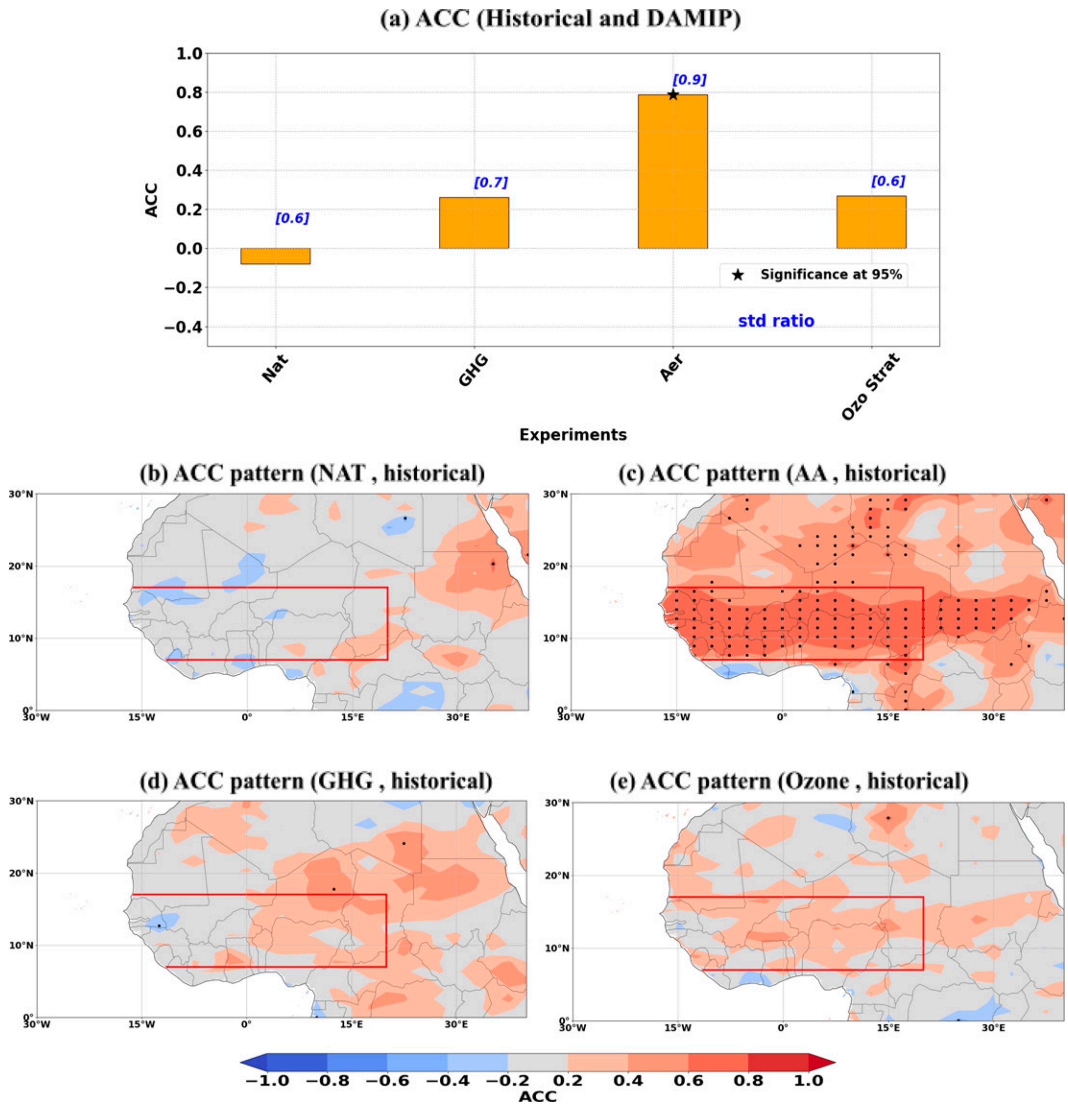

FIG. 7. (a) ACC of Sahel precipitation (JAS) between Historical and DAMIP experiments (Ens 10). Blue numbers show the ratio of standard deviations of the Sahel index between the DAMIP experiments and the Historical one. The 95% significant correlation is marked by an asterisk (*). (b)–(e) As in (a), but for individual grid points. ACC patterns between ensembles mean (Ens 10) of historical and DAMIP experiences as natural forcing (NAT), anthropogenic aerosol forcing (AA), greenhouse gas forcing (GHG), and stratospheric ozone forcing (Ozone), respectively. The 95% significant correlation is marked by dots. More information on the significance test used in the sections where this figure is described.

heat low (SHL) which is strongly coupled to the monsoon in this region (Shekhar and Boos 2017). This latter is diagnosed in this study as a maximum low-level atmospheric thickness (LLAT) that can be estimated as the difference between geopotential height at 700 hPa and at 925 hPa (i.e., ZG700 − ZG925), as in Lavaysse et al. (2009), Monerie et al. (2020a), and Shekhar and Boos (2017). On average, the SHL's ascent branch is located poleward of the ascending branch of the deep ITCZ (Shekhar and Boos 2017). In the piControl simulation, during intense WAM phases, the SHL exhibits a northward shift (Fig. 8d), which may be due to the SST pattern.

In the forced AA ensemble mean (Fig. 8c), the SST pattern associated with the averaged Sahel rainfall shows an interhemispheric dipole similar to the one obtained in the unforced simulation (Fig. 8b), albeit with a reduced area of statistically significant correlations, in particular in the North Atlantic Ocean and the Mediterranean Sea. Note that this picture shows an average influence of the ocean on the Sahel rainfall over the whole century. This approach differs and complements the recent study by Hirasawa et al. (2022), which gives a much more detailed description of the influence of the various basins over specific periods of the late twentieth century.

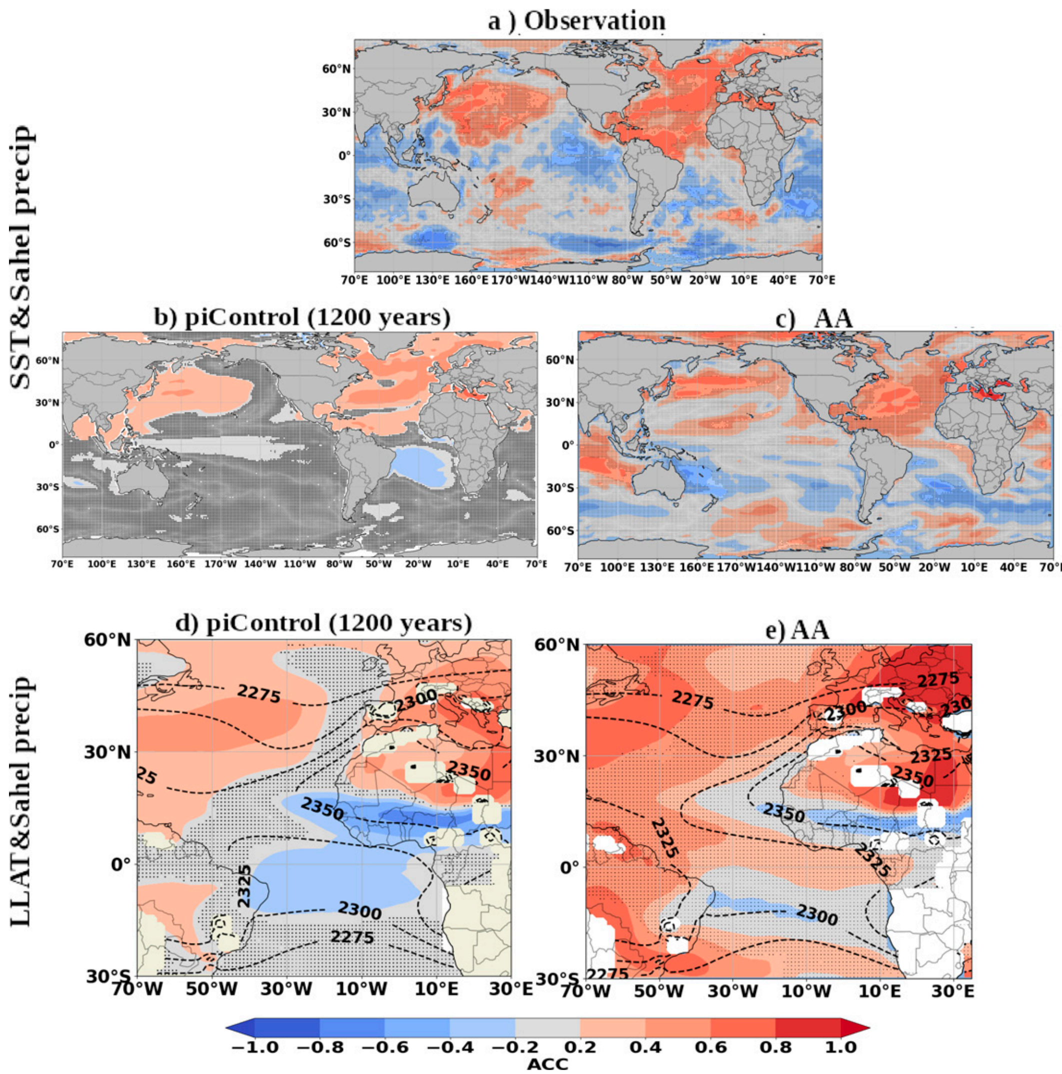

FIG. 8. ACC between the average Sahel precipitation (JAS) and sea surface temperature (SST; annual) and low-level atmospheric thickness (JAS) at each grid point for the period 1901–2014 from different datasets: from (a) CRU and HadISST observations, (b),(d) 1200-yr piControl, and (c),(e) the ensemble mean (Ens 10) of anthropogenic aerosol forcing (AA), respectively. The grid points where the correlation is not significant at 95% are marked by black dots. More information on the significance test used in the sections where this figure is described. The dashed black contours in (d) and (e) represent the annual climatology of the low-level atmospheric thickness. All fields have been linearly detrended before the computation.

Furthermore, the response of the LLAT in the AA ensemble is also consistent with the one found in the unforced simulation in particular over North Africa, the Mediterranean Sea, and southwest Europe (Fig. 8e). This northward shift of the SHL, together with the northward shift of the ITCZ over the Atlantic and adjacent continental areas (not shown) and the similarities between the SST patterns in both simulations, suggests that the mechanisms are similar and thus that part of the effect of the AA on Sahel rainfall is mediated through SSTs. By influencing the SSTs over the North Atlantic and the Mediterranean Sea, the AA would alter the summer migration of the ITCZ, and hence Sahel rainfall.

5. Discussion and conclusions

In this study, the contribution of the effect of internal variability and external forcings on low-frequency modulations of Sahel rainfall during the twentieth century was quantified using the observations and piControl and Historical experiments of 12 CMIP6 models and the DAMIP experiment of the IPSL-CM6A-LR model.

We first showed that the seasonal rainfall cycle in the Sahel in the historical ensembles of the CMIP6 models is relatively realistic but with an underestimate of the northward migration of the summer monsoon (JAS). In agreement with Klutse et al. (2021), this bias, also identified in the CMIP5 ensembles

(Monerie et al. 2020b), is differently represented among the CMIP6 models. To take this bias into account, we have proposed an adaptive physical definition of the Sahel region in coupled model simulations. In the observations, this region is characterized by meridional limits extending from the maximum rainfall in the south (10°N) to a latitude where no further rain takes place (less than 0.5 mm day^{-1}) in the north (20°N). Applying the same rainfall-based physical limits to the models, various latitudinal limits are obtained. The characterization of the rainy Sahel region proposed in this study is more physically based than the standard definitions and could thus be useful for other studies using coupled climate models. In the end, in spite of this adaptive definition, the maximum climatological simulated rainfall amounts are overestimated in the models as compared to the observation, except in NorCPM1, GISS-E2-1-G, and MPI-ESM1-2.

We then analyzed the observed and simulated low-frequency modulations of Sahel rainfall by evaluating the amplitude of the simulated variability and its synchrony to the observations over the whole twentieth century. In terms of variability amplitude, our results showed that, with the exception of MIROC6, all of the CMIP6 models used here underestimate the observed variability over the twentieth century. This underestimation identified in previous CMIP exercises (e.g., Rodríguez-Fonseca et al. 2011; Joly et al. 2007; Kucharski et al. 2013; Biasutti 2013) is thus not corrected in the new generation of models (CMIP6). To quantify separately the contribution of internal and externally forced variability on the simulated amplitude of the Sahel rainfall decadal modulations, the ensemble average of the historical simulations and the residual internal variability were respectively compared to the observations. With this analysis, we showed that the effect of internal variability explains the majority of the simulated amplitude in all models except the INM-CM5-0 model. Thus, the underestimation of the amplitude observed in these CMIP6 models could be due in part to the underestimation of the amplitude of simulated internal variability, as suggested in the North Atlantic region by Kim et al. (2018) and Yan et al. (2019). It also could be impacted by the precision with which the vegetation–atmosphere feedback is parameterized (Giannini et al. 2003; Zeng et al. 1999) or the coarseness of the model grid (Vellinga et al. 2016). Furthermore, although small, the external forcings play a nonnegligible role.

In terms of synchrony, our results clearly showed that in the CMIP6 ensemble, the internal variability is weakly correlated with the observations, while the external forcings induce low-frequency precipitation positively correlated with the observations. However, these correlations are significant only for 1/3 of the models, notably IPSL-CM6A-LR, INM-CM5-0, MRI-ESM2-0, and GISS-E2-1-G. This indicates a significant contribution of external forcings on the Sahel precipitation modulations for these few CMIP6 models, and probably not for the others.

To estimate the role of individual forcings for setting this synchrony, when it exists, we have analyzed DAMIP experiments. Unfortunately, focusing on models that performed at least 10 members as detailed in the section 2a, this analysis has been only possible with the IPSL-CM6A-LR model. The forced low-frequency modulations of the Sahel rainfall in the historical ensemble of 32 members performed with this model are significantly correlated with observations, especially over the western Sahel and part of the eastern Sahel. In spite of possible spurious influence of internal variability, the historical ensemble formed of the 10 first members confirms these results. The latter is thus used for subsequent comparison with the 10-member ensemble of DAMIP simulations, as they are started from the same initial conditions taken from the piControl run. In agreement with recent studies such as Herman et al. (2020) and Zhang et al. (2022), we find furthermore that in this model, the forced modulations of the Sahel precipitation over the whole twentieth century are mostly due to the anthropogenic aerosols (AA). A comparison of the structure of SST, rainfall, and the low-level atmospheric thickness associated with Sahel rainfall decadal modulations in observations, in the piControl simulation, and in the ensemble of simulations forced by the AA suggests that at least a part of the decadal modulation of Sahel rainfall in response to AA is mediated by the SST response to AA emissions. Our results suggest that the AA impacts the North Atlantic and Mediterranean Sea SSTs, which in turn affect Sahel rainfall through the northward shift of the Atlantic ITCZ and the Saharan heat low. This conclusion is consistent with previous works suggesting that the response of North Atlantic SST to AA could influence Sahel rainfall modulations during the twentieth century (e.g., Booth et al. 2012; Rotstayn and Lohmann 2002). We underline that here we show that this effect is strong enough to be detected on average over the whole twentieth century.

As we have seen above, the forced signal is significantly and not significantly correlated with the observations in 1/3 and 2/3 of the models used in this study, respectively. All these correlations could be influenced by the uncertainty of the response to external forcings in these models. Of all external forcings, climate response to AA is the most uncertain due to their spatial variation, short atmospheric lifetime, and complex interaction with clouds (Boucher et al. 2013; Bellouin et al. 2020; Smith et al. 2020). This uncertainty can be quantified by analyzing the processes driving long-term changes in global mean surface temperature via the effective radiative forcing index (ERF) in CMIP6 models (Smith et al. 2020). The range of AA ERF in the CMIP6 models estimates from 1850 to 2014 varies from -1.37 to -0.63 W m^{-2} (Smith et al. 2020). Compared to the AR5 assessment ((Shindell et al. 2015), there is a stronger negative AA ERF in CMIP6 (-1.01 W m^{-2} in CMIP6 for 1850–2014 versus -0.72 W m^{-2} in AR5 for 1850–2011). In IPSL-CM6A-LR, the model version in which AA forcing was shown to have a significant effect on the decadal modulation of the Sahel rainfall throughout the twentieth century, the ERF of AA amounts to approximately -0.6 W m^{-2} (Boucher et al. 2020; Mignot et al. 2021). This value is smaller than that of the other 18 CMIP6 models used by Smith et al. (2020), which may suggest that the significant response to AA forcing is not due to an overestimation of the AA forcing in this model.

Furthermore, although we have evidence supporting the hypothesis that for the IPSL-CM6A-LR model part of the impact of AA on the decadal variability of Sahel rainfall is mediated by SSTs, we have not quantified the role played by the direct atmospheric and ocean-mediated components (Dong and Sutton 2015; Hirasawa et al. 2020; Zhang et al. 2022). Hirasawa et al. (2022) attempted such separation using dedicated experiments using AGCM models. They attributed the dry period and a part of recent recovery of Sahel rainfall during the second half of the twentieth century to the direct (i.e., non-ocean-mediated) and ocean-mediated atmospheric responses, respectively. However, such AGCM experiments lack relevant physical processes such as ocean–atmosphere feedbacks, which are likely important for shaping the tropical Atlantic SST pattern and, thus, for modulating Sahel rainfall (Zhang et al. 2019, and references therein). Thus, future studies may imply the design of dedicated coupled sensitivity experiments in order to dig in more detail into these mechanisms. In addition, the analysis of the role of dynamic and thermodynamic processes could also help shed light on the effects of aerosols on modulating Sahel rainfall (Li et al. 2018).

Finally, there is a current debate on the ultimate causes for the recent recovery of Sahel rainfall at the end of the twentieth century with some studies pointing to the changes in anthropogenic aerosols as the main factor (Herman et al. 2020; Hirasawa et al. 2020; Monerie et al. 2022), while others suggest a more dominant role of GHG (Dong and Sutton 2015; Giannini and Kaplan 2019). Regardless of the current domination of GHG or AA over Sahel rainfall variability, GHG emissions are expected to become more and more dominant in the future (IPCC 2021). We may thus anticipate that the drivers of decadal modulations of the Sahel rainfall will evolve in the future.

Acknowledgments. This work was supported by the PDI/MSC (Programme Doctoral International: Modélisation des Systèmes Complexes), the scholarship of SCAC (Service de Coopération et d'Action Culturelle), and the ERASMUS+ programme through action KA107. This work was also supported by the Laboratoire Mixte International ECLAIRS2 (IRD), the UCM XVII call for cooperation and sustainable development, and the Ambassade de France en Espagne. EM also acknowledges the European Commission TRIATLAS (No. 817578), NextGEMS (No. 101003470), and the Spanish Ministry of Science and Competitiveness DISTROPIA (PID2021-125806NB-I00) projects. JM acknowledges the support of the JPI climate/JPI ocean project (ANR-19-JPOC-003).

REFERENCES

Bellomo, K., L. N. Murphy, M. A. Cane, A. C. Clement, and L. M. Polvani, 2018: Historical forcings as main drivers of the Atlantic multidecadal variability in the CESM large ensemble. *Climate Dyn.*, **50**, 3687–3698, https://doi.org/10.1007/s00382-017-3834-3.

Bellouin, N., and Coauthors, 2020: Bounding global aerosol radiative forcing of climate change. *Rev. Geophys.*, **58**, e2019RG000660, https://doi.org/10.1029/2019RG000660.

Berntell, E., Q. Zhang, L. Chafik, and H. Körnich, 2018: Representation of multidecadal Sahel rainfall variability in 20th century reanalyses. *Sci. Rep.*, **8**, 10937, https://doi.org/10.1038/s41598-018-29217-9.

Bethke, I., and Coauthors, 2021: NorCPM1 and its contribution to CMIP6 DCPP. *Geosci. Model Dev.*, **14**, 7073–7116, https://doi.org/10.5194/gmd-14-7073-2021.

Biasutti, M., 2013: Forced Sahel rainfall trends in the CMIP5 archive: Forced rainfall trends in the Sahel. *J. Geophys. Res.*, **118**, 1613–1623, https://doi.org/10.1002/jgrd.50206.

——, 2019: Rainfall trends in the African Sahel: Characteristics, processes, and causes. *Wiley Interdiscip. Rev.: Climate Change*, **10**, e591, https://doi.org/10.1002/wcc.591.

——, and A. Giannini, 2006: Robust Sahel drying in response to late 20th century forcings. *Geophys. Res. Lett.*, **33**, L11706, https://doi.org/10.1029/2006GL026067.

——, and Coauthors, 2018: Global energetics and local physics as drivers of past, present and future monsoons. *Nat. Geosci.*, **11**, 392–400, https://doi.org/10.1038/s41561-018-0137-1.

Bonnet, R., and Coauthors, 2021: Increased risk of near term global warming due to a recent AMOC weakening. *Nat. Commun.*, **12**, 6108, https://doi.org/10.1038/s41467-021-26370-0.

Booth, B. B. B., N. J. Dunstone, P. R. Halloran, T. Andrews, and N. Bellouin, 2012: Aerosols implicated as a prime driver of twentieth-century North Atlantic climate variability. *Nature*, **484**, 228–232, https://doi.org/10.1038/nature10946.

Boucher, O., and Coauthors, 2013: Clouds and aerosols. *Climate Change 2013: The Physical Science Basis*, T. F. Stocker et al., Eds., Cambridge University Press, 571–657.

——, and Coauthors, 2020: Presentation and evaluation of the IPSL-CM6A-LR climate model. *J. Adv. Model. Earth Syst.*, **12**, e2019MS002010, https://doi.org/10.1029/2019MS002010.

Danabasoglu, G., and Coauthors, 2020: The Community Earth System Model version 2 (CESM2). *J. Adv. Model. Earth Syst.*, **12**, e2019MS001916. https://doi.org/10.1029/2019MS001916.

Dong, B., and R. Sutton, 2015: Dominant role of greenhouse-gas forcing in the recovery of Sahel rainfall. *Nat. Climate Change*, **5**, 757–760, https://doi.org/10.1038/nclimate2664.

Döscher, R., and Coauthors, 2022: The EC-Earth3 Earth system model for the Coupled Model Intercomparison Project 6. *Geosci. Model Dev.*, **15**, 2973–3020, https://doi.org/10.5194/gmd-15-2973-2022.

Ebisuzaki, W., 1997: A method to estimate the statistical significance of a correlation when the data are serially correlated. *J. Climate*, **10**, 2147–2153, https://doi.org/10.1175/1520-0442(1997)010<2147:AMTETS>2.0.CO;2.

Eyring, V., S. Bony, G. A. Meehl, C. A. Senior, B. Stevens, R. J. Stouffer, and K. E. Taylor, 2016: Overview of the Coupled Model Intercomparison Project Phase 6 (CMIP6) experimental design and organization. *Geosci. Model Dev.*, **9**, 1937–1958, https://doi.org/10.5194/gmd-9-1937-2016.

Folland, C. K., T. N. Palmer, and D. E. Parker, 1986: Sahel rainfall and worldwide sea temperatures, 1901–85. *Nature*, **320**, 602–607, https://doi.org/10.1038/320602a0.

Gaetani, M., C. Flamant, S. Bastin, S. Janicot, C. Lavaysse, F. Hourdin, P. Braconnot, and S. Bony, 2017: West African monsoon dynamics and precipitation: The competition between global SST warming and CO_2 increase in CMIP5 idealized simulations. *Climate Dyn.*, **48**, 1353–1373, https://doi.org/10.1007/s00382-016-3146-z.

Giannini, A., and A. Kaplan, 2019: The role of aerosols and greenhouse gases in Sahel drought and recovery. *Climatic Change*, **152**, 449–466, https://doi.org/10.1007/s10584-018-2341-9.

——, R. Saravanan, and P. Chang, 2003: Oceanic forcing of Sahel rainfall on interannual to interdecadal time scales. *Science*, **302**, 1027–1103, https://doi.org/10.1126/science.1089357.

Gillett, N. P., and Coauthors, 2016: The Detection and Attribution Model Intercomparison Project (DAMIP v1.0) contribution to CMIP6. *Geosci. Model Dev.*, **9**, 3685–3697, https://doi.org/10.5194/gmd-9-3685-2016.

Haarsma, R. J., F. M. Selten, S. L. Weber, and M. Kliphuis, 2005: Sahel rainfall variability and response to greenhouse warming. *Geophys. Res. Lett.*, **32**, L17702, https://doi.org/10.1029/2005GL023232.

Harris, I., T. J. Osborn, P. Jones, and D. Lister, 2020: Version 4 of the CRU TS monthly high-resolution gridded multivariate climate dataset. *Sci. Data*, **7**, 109, https://doi.org/10.1038/s41597-020-0453-3.

Herman, R. J., A. Giannini, M. Biasutti, and Y. Kushnir, 2020: The effects of anthropogenic and volcanic aerosols and greenhouse gases on twentieth century Sahel precipitation. *Sci. Rep.*, **10**, 12203, https://doi.org/10.1038/s41598-020-68356-w.

Hirasawa, H., P. J. Kushner, M. Sigmond, J. Fyfe, and C. Deser, 2020: Anthropogenic aerosols dominate forced multidecadal Sahel precipitation change through distinct atmospheric and oceanic drivers. *J. Climate*, **33**, 10 187–10 204, https://doi.org/10.1175/JCLI-D-19-0829.1.

——, ——, ——, ——, and ——, 2022: Evolving Sahel rainfall response to anthropogenic aerosols driven by shifting regional oceanic and emission influences. *J. Climate*, **35**, 3181–3193, https://doi.org/10.1175/JCLI-D-21-0795.1.

Hourdin, F., C. Rio, A. Jam, A. Traore, and I. Musat, 2020: Convective boundary layer control of the sea surface temperature in the tropics. *J. Adv. Model. Earth Syst.*, **12**, e2019MS001988, https://doi.org/10.1029/2019MS001988.

IPCC, 2021: Summary for policymakers. *Climate Change 2021: The Physical Science Basis*, V. P. Masson-Delmotte, et al., Eds., 3−32, https://doi.org/10.1017/9781009157896.001.

Jiang, W., G. Gastineau, and F. Codron, 2021: Multicentennial variability driven by salinity exchanges between the Atlantic and the Arctic Ocean in a coupled climate model. *J. Adv. Model. Earth Syst.*, **13**, e2020MS002366, https://doi.org/10.1029/2020MS002366.

Joly, M., A. Voldoire, H. Douville, P. Terray, and J.-F. Royer, 2007: African monsoon teleconnections with tropical SSTs: Validation and evolution in a set of IPCC4 simulations. *Climate Dyn.*, **29** (1), 1–20, https://doi.org/10.1007/s00382-006-0215-8.

Kandji, S. T., L. Verchot, and J. Mackensen, 2006: Climate change and variability in the Sahel region: Impacts and adaptation strategies in the agricultural sector. United Nations Environmental Programme and World Agroforestry Centre, 48 pp., http://apps.worldagroforestry.org/downloads/Publications/PDFS/B14549.pdf.

Kang, S. M., 2020: Extratropical influence on the tropical rainfall distribution. *Curr. Climate Change Rep.*, **6**, 24–36, https://doi.org/10.1007/s40641-020-00154-y.

——, I. M. Held, D. M. W. Frierson, and M. Zhao, 2008: The response of the ITCZ to extratropical thermal forcing: Idealized slab-ocean experiments with a GCM. *J. Climate*, **21**, 3521–3532, https://doi.org/10.1175/2007JCLI2146.1.

Kay, J. E., and Coauthors, 2015: The Community Earth System Model (CESM) large ensemble project: A community resource for studying climate change in the presence of internal climate variability. *Bull. Amer. Meteor. Soc.*, **96**, 1333–1349, https://doi.org/10.1175/BAMS-D-13-00255.1.

Kim, W. M., S. G. Yeager, and G. Danabasoglu, 2018: Key role of internal ocean dynamics in Atlantic multidecadal variability during the last half century. *Geophys. Res. Lett.*, **45**, 13 449–13 457, https://doi.org/10.1029/2018GL080474.

Klutse, N. A. B., and Coauthors, 2021: The climatic analysis of summer monsoon extreme precipitation events over West Africa in CMIP6 simulations. *Earth Syst. Environ.*, **5**, 25–41, https://doi.org/10.1007/s41748-021-00203-y.

Kucharski, F., N. Zeng, and E. Kalnay, 2013: A further assessment of vegetation feedback on decadal Sahel rainfall variability. *Climate Dyn.*, **40**, 1453–1466, https://doi.org/10.1007/s00382-012-1397-x.

Lavaysse, C., C. Flamant, S. Janicot, D. J. Parker, J.-P. Lafore, B. Sultan, and J. Pelon, 2009: Seasonal evolution of the West African heat low: A climatological perspective. *Climate Dyn.*, **33**, 313–330, https://doi.org/10.1007/s00382-009-0553-4.

Lawrence, D. M., and Coauthors, 2016: The Land Use Model Intercomparison Project (LUMIP) contribution to CMIP6: Rationale and experimental design. *Geosci. Model Dev.*, **9**, 2973–2998, https://doi.org/10.5194/gmd-9-2973-2016.

Lebel, T., and Ali, A., 2009: Recent trends in the central and western Sahel rainfall regime (1990–2007). *J. Hydrol.*, **375**, 52–64, https://doi.org/10.1016/j.jhydrol.2008.11.030.

Li, X., M. Ting, and D. E. Lee, 2018: Fast adjustments of the Asian summer monsoon to anthropogenic aerosols. *Geophys. Res. Lett.*, **45**, 1001–1010, https://doi.org/10.1002/2017GL076667.

Lu, J., 2009: The dynamics of the Indian Ocean sea surface temperature forcing of Sahel drought. *Climate Dyn.*, **33**, 445–460, https://doi.org/10.1007/s00382-009-0596-6.

Maher, N., S. Milinski, and R. Ludwig, 2021: Large ensemble climate model simulations: Introduction, overview, and future prospects for utilising multiple types of large ensemble. *Earth Syst. Dyn.*, **12**, 401–418, https://doi.org/10.5194/esd-12-401-2021.

Mann, M. E., B. A. Steinman, D. J. Brouillette, and S. K. Miller, 2021: Multidecadal climate oscillations during the past millennium driven by volcanic forcing. *Science*, **371**, 1014–1019, https://doi.org/10.1126/science.abc5810.

Martin, E. R., C. Thorncroft, and B. B. B. Booth, 2014: The multidecadal Atlantic SST–Sahel rainfall teleconnection in CMIP5 simulations. *J. Climate*, **27**, 784–806, https://doi.org/10.1175/JCLI-D-13-00242.1.

Mauritsen, T., and Coauthors, 2019: Developments in the MPI-M Earth System Model version 1.2 (MPI-ESM1.2) and its response to increasing CO_2. *J. Adv. Model. Earth Syst.*, **11**, 998–1038, https://doi.org/10.1029/2018MS001400.

Meyer-Christoffer, A., A. Becker, P. Finger, U. Schneider, and M. Ziese, 2018: GPCC precipitation climatology version 2018 at 0.5°: Monthly land-surface precipitation climatology for every month and the total year from rain-gauges built on GTS-based and historic data: Globally gridded monthly totals. GPCC, accessed January 2020, https://doi.org/10.5676/DWD_GPCC/CLIM_M_V2018_050.

Mignot, J., and Coauthors, 2021: The tuning strategy of IPSL-CM6A-LR. *J. Adv. Model. Earth Syst.*, **13**, e2020MS002340, https://doi.org/10.1029/2020MS002340.

Miller, R. L., and Coauthors, 2021: CMIP6 historical simulations (1850–2014) with GISS-E2.1. *J. Adv. Model. Earth Syst.*, **13**, e2019MS002034, https://doi.org/10.1029/2019MS002034.

Mohino, E., S. Janicot, and J. Bader, 2011: Sahel rainfall and decadal to multi-decadal sea surface temperature variability. *Climate Dyn.*, **37**, 419–440, https://doi.org/10.1007/s00382-010-0867-2.

Monerie, P.-A., E. Sanchez-Gomez, M. Gaetani, E. Mohino, and B. Dong, 2020a: Future evolution of the Sahel precipitation zonal contrast in CESM1. *Climate Dyn.*, **55**, 2801–2821, https://doi.org/10.1007/s00382-020-05417-w.

——, C. M. Wainwright, M. Sidibe, and A. A. Akinsanola, 2020b: Model uncertainties in climate change impacts on Sahel precipitation in ensembles of CMIP5 and CMIP6 simulations. *Climate Dyn.*, **55**, 1385–1401, https://doi.org/10.1007/s00382-020-05332-0.

——, L. J. Wilcox, and A. G. Turner, 2022: Effects of anthropogenic aerosol and greenhouse gas emissions on Northern Hemisphere monsoon precipitation: Mechanisms and uncertainty. *J. Climate*, **35**, 2305–2326, https://doi.org/10.1175/JCLI-D-21-0412.1.

Nicholson, S. E., 1983: Sub-Saharan rainfall in the years 1976–80: Evidence of continued drought. *Mon. Wea. Rev.*, **111**, 1646–1654, https://doi.org/10.1175/1520-0493(1983)111<1646:SSRITY>2.0.CO;2.

Park, J., J. Bader, and D. Matei, 2016: Anthropogenic Mediterranean warming essential driver for present and future Sahel rainfall. *Nat. Climate Change*, **6**, 941–945, https://doi.org/10.1038/nclimate3065.

Pascoe, C., B. N. Lawrence, E. Guilyardi, M. Juckes, and K. E. Taylor, 2019: Designing and documenting experiments in CMIP6. *Geosci. Model Dev. Discuss.*, https://doi.org/10.5194/gmd-2019-98.

Rayner, N. A., D. E. Parker, E. B. Horton, C. K. Folland, L. V. Alexander, D. P. Rowell, E. C. Kent, and A. Kaplan, 2003: Global analyses of sea surface temperature, sea ice, and night marine air temperature since the late nineteenth century. *J. Geophys. Res.*, **108**, 4407, https://doi.org/10.1029/2002JD002670.

Rodríguez-Fonseca, B., and Coauthors, 2011: Interannual and decadal SST-forced responses of the West African monsoon. *Atmos. Sci. Lett.*, **12**, 67–74, https://doi.org/10.1002/asl.308.

——, and Coauthors, 2015: Variability and predictability of West African droughts: A review on the role of sea surface temperature anomalies. *J. Climate*, **28**, 4034–4060, https://doi.org/10.1175/JCLI-D-14-00130.1.

Rotstayn, L. D., and U. Lohmann, 2002: Tropical rainfall trends and the indirect aerosol effect. *J. Climate*, **15**, 2103–2116, https://doi.org/10.1175/1520-0442(2002)015<2103:TRTATI>2.0.CO;2.

Rowell, D. P., 2003: The impact of Mediterranean SSTs on the Sahelian rainfall season. *J. Climate*, **16**, 849–862, https://doi.org/10.1175/1520-0442(2003)016<0849:TIOMSO>2.0.CO;2.

Scaife, A., and D. Smith, 2018: A signal-to-noise paradox in climate science. *npj Climate Atmos. Sci.*, **1**, 28, https://doi.org/10.1038/s41612-018-0038-4.

Schneider, T., T. Bischoff, and G. H. Haug, 2014: Migrations and dynamics of the intertropical convergence zone. *Nature*, **513**, 45–53, https://doi.org/10.1038/nature13636.

Shekhar, R., and W. R. Boos, 2017: Weakening and shifting of the Saharan shallow meridional circulation during wet years of the West African monsoon. *J. Climate*, **30**, 7399–7422, https://doi.org/10.1175/JCLI-D-16-0696.1.

Shindell, D. T., G. Faluvegi, L. Rotstayn, and G. Milly, 2015: Spatial patterns of radiative forcing and surface temperature response. *J. Geophys. Res. Atmos.*, **120**, 5385–5403, https://doi.org/10.1002/2014JD022752.

Smith, C. J., and Coauthors, 2020: Effective radiative forcing and adjustments in CMIP6 models. *Atmos. Chem. Phys.*, **20**, 9591–9618, https://doi.org/10.5194/acp-20-9591-2020.

Swart, N. C., and Coauthors, 2019: The Canadian Earth System Model version 5 (CanESM5.0.3). *Geosci. Model Dev.*, **12**, 4823–4873, https://doi.org/10.5194/gmd-12-4823-2019.

Tatebe, H., and Coauthors, 2019: Description and basic evaluation of simulated mean state, internal variability, and climate sensitivity in MIROC6. *Geosci. Model Dev.*, **12**, 2727–2765, https://doi.org/10.5194/gmd-12-2727-2019.

Thorncroft, C. D., H. Nguyen, C. Zhang, and P. Peyrillé, 2011: Annual cycle of the West African monsoon: Regional circulations and associated water vapour transport. *Quart. J. Roy. Meteor. Soc.*, **137**, 129–147, https://doi.org/10.1002/qj.728.

Undorf, S., D. Polson, M. A. Bollasina, Y. Ming, A. Schurer, and G. C. Hegerl, 2018: Detectable impact of local and remote anthropogenic aerosols on the 20th century changes of West African and South Asian monsoon precipitation: D&A aerosols and monsoon precipitation. *J. Geophys. Res. Atmos.*, **123**, 4871–4889, https://doi.org/10.1029/2017JD027711.

Vellinga, M., M. Roberts, P. L. Vidale, M. S. Mizielinski, M.-E. Demory, R. Schiemann, J. Strachan, and C. Bain, 2016: Sahel decadal rainfall variability and the role of model horizontal resolution. *Geophys. Res. Lett.*, **43**, 326–333, https://doi.org/10.1002/2015GL066690.

Villamayor, J., and E. Mohino, 2015: Robust Sahel drought due to the interdecadal Pacific Oscillation in CMIP5 simulations. *Geophys. Res. Lett.*, **42**, 1214–1222, https://doi.org/10.1002/2014GL062473.

——, ——, M. Khodri, J. Mignot, and S. Janicot, 2018: Atlantic control of the late nineteenth-century Sahel humid period. *J. Climate*, **31**, 8225–8240, https://doi.org/10.1175/JCLI-D-18-0148.1.

Voldoire, A., and Coauthors, 2019: Evaluation of CMIP6DECK experiments with CNRM-CM6-1. *J. Adv. Model. Earth Syst.*, **11**, 2177–2213, https://doi.org/10.1029/2019MS001683.

Volodin, E. M., and Coauthors, 2018: Simulation of the modern climate using the INM-CM48 climate model. *Russ. J. Numer. Anal. Math. Modell.*, **33**, 367–374, https://doi.org/10.1515/rnam-2018-0032.

Weisheimer, A., and Coauthors, 2019: How confident are predictability estimates of the winter North Atlantic oscillation? *Quart. J. Roy. Meteor. Soc.*, **145** (Suppl. 1), 140–159, https://doi.org/10.1002/qj.3446.

Yan, X., R. Zhang, and T. R. Knutson, 2019: A multivariate AMV index and associated discrepancies between observed and CMIP5 externally forced AMV. *Geophys. Res. Lett.*, **46**, 4421–4431, https://doi.org/10.1029/2019GL082787.

Yukimoto, S., and Coauthors, 2019: The Meteorological Research Institute Earth system model version 2.0, MRI-ESM2.0: Description and basic evaluation of the physical component. *J Meteor. Soc. Japan*, https://doi.org/10.2151/jmsj.2019-051.

Zeng, N., J. D. Neelin, K. M. Lau, and C. J. Tucker, 1999: Enhancement of interdecadal climate variability in the Sahel by vegetation interaction. *Science*, **286**, 1537–1540, https://doi.org/10.1126/science.286.5444.1537.

Zhang, R., R. Sutton, G. Danabasoglu, Y. Kwon, R. Marsh, S. G. Yeager, D. E. Amrhein, and C. M. Little, 2019: A review of the role of the Atlantic meridional overturning circulation in Atlantic multidecadal variability and associated climate impacts. *Rev. Geophys.*, **57**, 316–375, https://doi.org/10.1029/2019RG000644.

Zhang, S., P. Stier, G. Dagan, and M. Wang, 2022: Anthropogenic aerosols modulated 20th-century Sahel rainfall variability via their impacts on North Atlantic sea surface temperature. *Geophys. Res. Lett.*, **49**, e2021GL095629, https://doi.org/10.1029/2021GL095629.

Ziehn, T., and Coauthors, 2020: The Australian Earth System Model: ACCESS-ESM1.5. *J. South. Hemisphere Earth Syst. Sci.*, **70**, 193–214, https://doi.org/10.1071/ES19035.ss